Available online at www.sciencedirect.com
SCIENCE DIRECT
International Journal of Mass Spectrometry 254 (2006) 70–84
International Journal of Mass Spectrometry
www.elsevier.com/locate/ijms

TOF-SIMS characterisation of spark-generated nanoparticles made from pairs of Ir–Ir and Ir–C electrodes

W. Szymczak [a], N. Menzel [a], W.G. Kreyling [b,c], K. Wittmaack [a,*]

[a] GSF-National Research Centre for Environment and Health, Institute of Radiation Protection, D-85758 Neuherberg, Germany
[b] GSF-National Research Centre for Environment and Health, Institute of Inhalation Biology, D-85758 Neuherberg, Germany
[c] GSF-National Research Centre for Environment and Health, Focus Network Aerosols and Health, D-85758 Neuherberg, Germany

Received 22 March 2006; received in revised form 11 May 2006; accepted 15 May 2006
Available online 15 June 2006

Abstract

This paper constitutes a comprehensive study on the use of time-of-flight secondary ion mass spectrometry (TOF-SIMS) for determining the composition of spark-generated nanoparticles as well as for deriving information on their size. This kind of nano-sized matter is often used in animal studies to explore and quantify lung inflammatory response to inhalation or instillation of insoluble particles. Two iridium samples, Ir(#1) and Ir(#2), were generated with a pair of electrodes made of pure iridium. A mixed C(Ir) sample was produced with one electrode of carbon and the other of iridium. The primary particles of Ir had a size ("diameter") $D_p \leq 5$ nm, but they were agglomerated in chain-type aggregates with different mean electrical mobility diameter, depending on the spark frequency. The atomic fraction of Ir in the C(Ir) particles was less than 1% ($D_p \sim 13$ nm). The generated particles were collected on cellulose acetate-nitrate filters. An Ir electrode with a polished surface served as a reference sample. SIMS analysis of negative secondary ions was performed under impact of 34 keV Ar^+. The mass spectra of the Ir samples revealed surprisingly high yields of cluster ions of the type Ir_kXY^-, with k up to 20 and XY indicating combinations of oxygen, nitrogen and carbon. A detailed evaluation of cluster composition based on the isotopic pattern of Ir revealed a high oxygen content in the particles located at the surface of fresh samples. The true oxygen content of these "oxide" particles appears to be reduced by preferential sputtering. Depth dependent information was derived by sputter erosion in between a series of TOF mass spectra. Surprisingly, the (primary) oxide particles in Ir(#1) featured a very high cross-section for sputter ejection, reminiscent of monolayer removal. The particles uncovered by sputtering were much larger and mostly made of carbon-rich Ir particles ("carbides"), with the addition of some nitrogen. Combined with the high cluster ion yields, the results suggest that the Ir oxide was contained in flakes or chunks with sizes as small as 1 nm or even less. The same or similar oxide species were present in Ir(#2), but piled up to thicker layers. Very similar Ir oxide and carbide particles were identified in the C(Ir) sample, but at a very low yield, roughly corresponding to the atomic fraction of Ir.

Keywords: Nanoparticle; Iridium; Carbon; Spark discharge; Mass spectrometry

1. Introduction

Atmospheric aerosol particles with lateral dimensions between 1 nm and 10 μm have received increasing scientific and public attention because of their impact in two distinctly different areas: (i) the possible counteracting effect on global warming [1] and (ii) the potential hazard for human health, including the danger of increased mortality [2]. The relevant phenomena are extremely difficult to understand because the aerosol particulate matter can be of natural and anthropogenic origin, featuring a very complex, size dependent composition [3]. In the field of adverse health effects due to the inhalation of aerosol particles, considerable interest is currently being devoted to 'nanoparticles' and 'ultrafine particles'. According to convention, the latter feature sizes ≤100 nm [4]. A corresponding, widely accepted definition for the term nanoparticles does not exist. An upper limit between 10 and 30 nm appears reasonable. On the low-end side one may consider 1 nm the minimum size an assembly of matter should have in all three directions to be referred to as a 'particle' (example: C_{60}). A significant if not large fraction of ambient nanoparticles and ultrafine particles is contained in vehicle exhaust

* Corresponding author. Tel.: +49 89 3187 2439; fax: +49 89 3187 3323.
E-mail address: wittmaack@gsf.de (K. Wittmaack).

1387-3806/$ – see front matter © 2006 Elsevier B.V. All rights reserved.
doi:10.1016/j.ijms.2006.05.010

[5,6], but a sizable fraction may also be of natural origin [7].

To reduce the complexity and variability of ambient particles in terms of composition and number concentration, animal studies into health effects are commonly performed by exposure to air that has been loaded with laboratory generated nanoparticles [8], often produced using spark discharges [9–11]. The standard method of characterising these particles is to measure their size distribution. This is done not directly but in terms of the particle's mobility in an electrical field [12]. The morphology of collected nanoparticles has been studied in some detail by transmission electron microscopy (TEM) [11,13]. Scanning electron microscopy (SEM) in combination with energy dispersive X-ray analysis (EDX) [14] and atomic force microscopy (AFM) were also used to characterise other types of laboratory generated particles [15–17] and agglomerates [18].

Up to now, comparatively little attention has been devoted to compositional analysis of nanoparticles. One exception is a recent multi-technique study [19] on the composition of soot particles produced either by a diesel engine or a graphite spark discharge. The analytical techniques included single-particle laser based mass spectrometry, secondary neutral mass spectrometry (SNMS), secondary ion mass spectrometry (SIMS), X-ray photoelectron spectrometry (XPS) and Fourier transform infrared (FTIR) spectrometry. The most detailed information on particle composition was obtained by SNMS depth profiling of samples collected in different size ranges using an impactor. Owing to large-area bombardment, the depth profiles provided information averaged over a very large number of particles. SIMS and SNMS had previously been applied to assess the composition of atmospheric aerosol samples [20–22]. Sample rotation was applied to improve the uniformity of sputter erosion of micrometer-sized particles [23]. Attempts have also been made to achieve single-particle analysis using focussed liquid metal ion beams available in commercial time-of-flight (TOF) SIMS systems. However, owing to the trade-off between mass and spatial resolution, the practical limit in lateral resolution was in the range 0.5–2 μm, or even higher [24–28].

At the GSF National Research Centre for Environment and Health the issue of possible adverse health effects due to the inhalation of ambient aerosol particles is a topic of prime concern. One research avenue is to study the fate of nanoparticles after their deposition in the lung of animals, e.g., rats. The question is whether the particles can be translocated from the deposition site into the blood system so that they may finally be ending up in critical organs like the liver, the heart or even the brain. An accurate determination of the concentration of the administered particles in the different organs requires the use of suitable radioactive markers. One isotope that has been found to be particularly useful in this respect is ^{192}Ir, a beta and gamma emitter with a half-life of 74 days [29,30]. Iridium nanoparticles can be produced conveniently in a spark discharge using pure metallic electrodes [11]. Even though nanoparticle production takes place in a flow of pure argon, one must expect that the emitted, thermally excited atoms, molecules and clusters will react with residual gases like oxygen, nitrogen and hydrocarbons. Calculated binding energies for chemisorption of O, N and C on Ir(111) exceed 3 eV [31]. Incorporation of these impurities in the surface layer or even the bulk of the growing Ir nanoparticles would change the reactivity of the particles in body liquids. IrO_2, for example, is known to feature high chemical inertness [32].

In view of the complete lack of knowledge concerning the composition of laboratory generated Ir nanoparticles, we have set out to perform the first comprehensive analysis of such particles by TOF-SIMS, after collection on a suitable filter. To assist interpretation of the TOF-SIMS data, the collected particles were also analysed by SEM and proton induced X-ray (PIXE) spectrometry.

2. Experiment

2.1. Particle generation and sample preparation

Nanoparticles were generated in a commercial spark generator (model GFG 1000, Palas) using electrodes of high-purity material. Details of the system have been described very recently [29,33]. Hence, only a brief summary is given here. Iridium nanoparticles were produced from electrodes of metallic iridium. In one of the experiments, the spark discharge was operated with one electrode made of carbon, the other of iridium, the aim being to produce carbon nanoparticles with embedded iridium marker atoms, preferably in the form of a sub-nanometer core, i.e., carbon–iridium particles with only carbon atoms at the surface.

The generated particles were carried away from the spark discharge in flowing high-purity (5N) argon. A small fraction of the particle laden gas flow was directed through a differential mobility particle analyser and a condensation particle counter for determining the size distributions, which were found to be unimodal and approximately of lognormal form [33]. The mean mobility diameters $\langle D \rangle$ of spark-generated particles are known to increase with increasing spark frequency ν [10,11]. The first Ir sample, labelled Ir(#1), was generated at a comparatively low frequency of 4 Hz, with $\langle D \rangle = 18$ nm, the second one, Ir(#2) at 330 Hz, with $\langle D \rangle = 74$ nm. The mixed C/Ir sample, labelled C(Ir) was produced at 4 Hz with $\langle D \rangle = 33$ nm. The distributions exhibited similar width, ∼0.2 on the logarithmic size scale. The major fraction of the generated particles was collected on cellulose acetate-nitrate (CA) filters with a nominal pore size of 0.8 μm (Millipore). To increase the deposition density, the particle collection area was reduced to 2 cm^2 by placing a diaphragm with four 8-mm-diameter apertures behind the CA filter.

The masses of the deposited layers were 260, 220 and 100 μg for Ir(#1), Ir(#2) and C(Ir), respectively (uncertainty ±10 μg), corresponding to areal mass densities of 130, 110 and 50 μg/cm^2, respectively. Assuming bulk mass densities (ρ(Ir) = 22.6 g/cm^3), the two Ir samples would have a thickness of 58 and 49 nm, respectively, if converted to compact layers. The three samples were also analysed by PIXE [34]. The mass of Ir in C(Ir) was found to be 12 μg, equivalent to 12% by mass or to an atomic fraction of only 0.85 at%. With ρ(graphite) = 2.15 g/cm^3, the mean bulk density of C(Ir) is

calculated as 2.32 g/cm^3. Converted to a compact layer, this sample would be 216 nm thick.

Sections of the particle loaded filter, 8 mm × 8 mm wide, were mounted on a target holder for SIMS analysis, held in place by a thin metallic diaphragm. A reference sample was prepared by cutting a small section off a cylindrical Ir electrode (diameter 0.7 mm), previously used in the spark generator. The front face of this sample was polished with 1-μm diamond paste to a shiny finish, rinsed with methanol and high-purity water and mounted in a dedicated target holder.

Previous TEM studies [11] have shown that spark-generated carbon and iridium particles are chain-type aggregates composed of very small primary particles with sizes of only a few nanometers. Owing to the large thickness of the CA filters, TEM analysis was not possible on the samples produced here for SIMS analysis. Hence, an attempt has been made to assess the mean primary particle size by making use of the information contained in the measured particle size distributions and the masses of the deposits. This approach turned out to work surprisingly well [33]. Assuming moderate branching of the chain-type aggregates so that their total length would correspond to three times the mobility diameter, the mean primary particle diameters turned out to be 3.5, 5.2 and 12.9 nm for Ir(#2), Ir(#1) and C(Ir), respectively (estimated uncertainty about 20%). The presence of a certain fraction of smaller primary particles could not be excluded. Very small iridium particles with a mean size of 2 nm have been found in iridium–carbon films prepared by simultaneous radio-frequency sputtering of iridium and carbon in a low-pressure argon atmosphere [35]. Primary particles with sizes between 1 and 4 nm can also be identified in TEM images of low-frequency spark-generated Ir described in another recent study [29]. These particles were somewhat too cautiously characterized as containing "substructures smaller than 5 nm".

2.2. TOF-SIMS system

TOF-SIMS analysis was performed with a homebuilt instrument, which, in its basic configuration, has been described some time ago [36]. Several improvements have been implemented since then [37,38]. The system consists of a small accelerator producing mass analysed beams, in this case 30 kV Ar^+, at a beam current of 50 nA. Pulsed ion bombardment of the sample was accomplished by rapidly sweeping the beam across an aperture, followed by bunching. The pulse width thus achieved was 3 ns. The angle between the axis of the final beam line and the surface normal of the sample was 60°. Near-target apertures served to produce a beam of rectangular shape, 0.7 mm wide in the plane of beam incidence and 0.3 mm wide normal to this plane. The secondary ions were accelerated in a two-step manner, in this study with the target at −4 kV, an intermediate electrode at −2 kV (target-to-electrode spacing 3.5 mm) and the drift section at ground potential. Owing to primary ion deflection in the extraction field between the target and the intermediate electrode, the actual impact angle of the ions, incident at a total energy of 34 keV, was about 57°. A special feature of the TOF system is the split drift tube, which allows the major fraction of the neutrals generated on flight by fragmentation [39] to be removed by tilting the second section a few degrees away from the first. The maximum flight time was set to slightly less than 50 μs (95,000 channels; mass range up to m/z 4000). Hence, the maximum repetition rate was 20 kHz. Mass spectra were acquired during impact of typically 1×10^7 primary ion pulses, with the anode of the detector at ground potential. The corresponding primary ion fluence was about 4×10^{12} ions/cm^2. By the time the experiments of this study were performed, the secondary ion beam line did not contain means for energy focussing like a reflectron. Furthermore, the instrument did not include an electron gun for charge compensation in the analysis of insulating samples.

To allow for TOF-SIMS measurements after sample exposure to primary ion fluences well beyond the low-damage ("static") limit, i.e., to remove material intermittently by exposure to comparatively long primary ion pulses, the electronics controlling pulse length and beam deflection were modified to the end that the sample could be bombarded with a raster scanned beam with a pulse length of about 150 ns, at repetition rates between 2 and 5 kHz. In the sputter mode, the digitally rastered beam was moved across an area of roughly 1 mm × 1 mm on the nanoparticle samples, but only about 0.5 mm × 0.5 mm on the Ir electrode.

The SIMS analysis chamber was evacuated by an ion pump (300 L/s). Pressures were measured at remote positions. The pressure at the target was estimated to range between 5 and 8×10^{-9} hPa.

2.3. Sample characterisation by SEM

Information on sample morphology was obtained by SEM (for SEM details see ref. [40]). Images taken in the region of macroscopically uniform iridium deposition are presented in Fig. 1 (deposition of a conducting layer not required). Panels (a) and (b) show the Ir(#1), panels (c) and (d) the Ir(#2) deposits; panels (a) and (c) relate to virgin samples, (b) and (d) to samples exposed to the maximum primary ion fluence applied in this study, 3×10^{14} and 4×10^{14} ions cm^{-2}, for Ir(#1) and Ir(#2), respectively. It is evident at first sight that, from the perspective of materials characterisation by secondary ion mass spectrometry, the samples constitute an outstanding, if not the ultimate challenge. Instead of a compact material with a well defined surface we had to deal with a very rough deposit of tiny particles piled up in rather irregular form. The images suggest that most of the collected matter came to rest on the front surface of the filter rather than in the pores, which make up the inner surfaces of the filter. Very long aggregates, much longer than the mean mobility diameter of the particles are observed. This finding implies that pronounced (additional) chain-type agglomeration took place during particle collection on the filter. The Ir(#2) sample was more densely covered with very long aggregates than the Ir(#1) sample. This could be due to the fact the as-produced chain-aggregates in Ir(#2) were much longer than in Ir(#1). Probably as a result of local pile-up of agglomerates during sampling, a significant fraction of the filter was not covered with particulate matter.

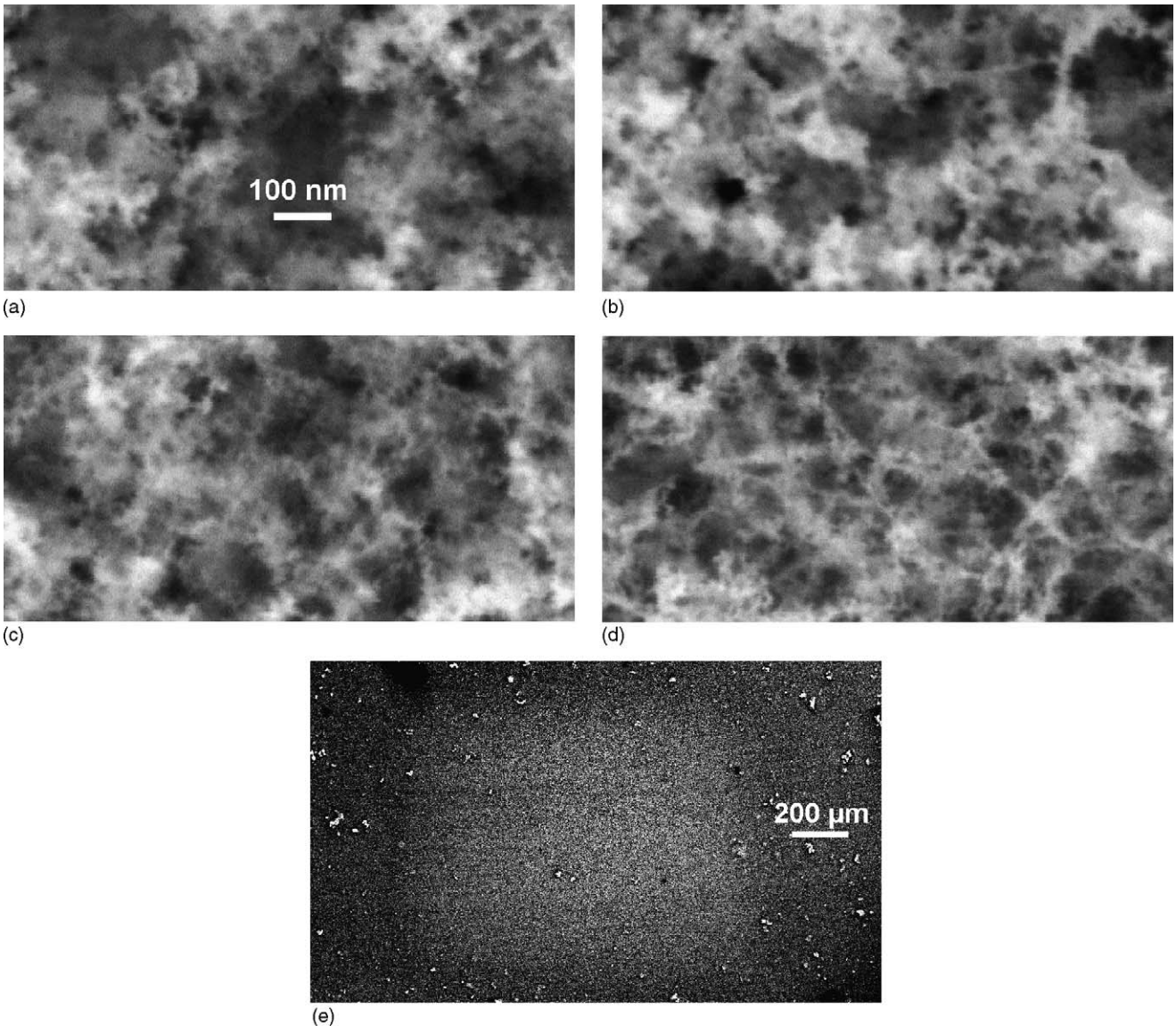

Fig. 1. SEM micrographs of iridium samples produced by collecting spark-generated particles with different mean mobility diameters on CA filters. (a and b) Ir(#1), (c and d) Ir(#2). (a and c) As-prepared samples, (b and d) after sputter erosion. All four images were taken at the same magnification. (e) Low-resolution image of sample Ir(#2) centred to the sputtered area.

At first sight there appears to be no significant difference between the virgin and the sputtered samples. A closer inspection of the images, however, shows that the contrast in the images is significantly better in the sputtered than in the virgin samples. In the virgin case, one has the impression that the sample was covered by some kind of mist or haze that prevented optimum identification of all particles present on the sample. The haze seems to be missing in the sputter eroded sections of the sample. One possible interpretation of this observation is that the virgin samples were (additionally) covered by a 'layer' of very small particles, which could not be resolved by the employed SEM instrument. The tiny particles were removed by sputtering more rapidly than the larger particles (and the aggregates) so that the latter became visible with better contrast once the haze had been removed. As shown in Fig. 1(e), the ion bombarded area is difficult to identify, another indication that only a small amount of sample material was removed by sputtering.

3. Results and discussion

3.1. TOF-SIMS spectra: overview

SIMS analysis of the samples was initially carried out in the positive as well as in the negative mode. The positive secondary ion spectra of the nanoparticle samples were characterised by very high $C_iH_j^+$ lines due to hydrocarbon surface contaminants (i, $j = 1, 2, 3, \ldots$) but rather low signals of Ir oxide and carbide. The latter species showed prominent peaks in the negative spectra. Hence, detailed measurements were carried out only in the negative mode. A compilation of mass spectra of virgin nanoparticle samples as well as of the Ir metal reference

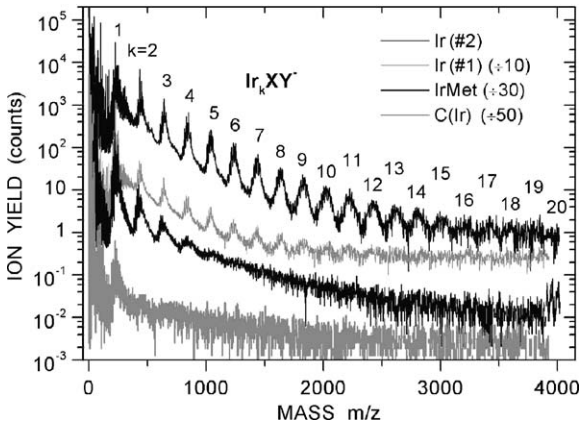

Fig. 2. Comparison of the TOF mass spectra of the four samples investigated in this study. The spectra reflect the composition at the surface of the fresh samples. To avoid excessive spectral overlap, three of the four spectra were scaled by the factors shown in parentheses.

sample is presented in Fig. 2. To avoid overlap of structural features, three of the four spectra were divided by appropriate factors (shown in parentheses). Even though the nanoparticles were collected on insulating filter material, charging under ion impact was not observed. Apparently, the particles featured sufficient electrical conductivity to allow efficient transport of the (pulsed) primary ion current to the metallic diaphragm surrounding the deposited matter. A similar sample of spark-generated carbon nanoparticles, made from pure graphite electrodes, did show severe charging in TOF-SIMS analysis so that meaningful spectra could not be obtained. The lack of charging with C(Ir) could indicate that a sizable fraction of the Ir atoms in that sample was present at the surface rather than in the "bulk" of the nanoparticles.

The most remarkable feature in the spectra of Fig. 2 is the wide range of molecular (cluster) ions of the type Ir_kXY^-, notably observed with samples Ir(#2) and Ir(#1) ("XY" indicate combinations of oxygen, nitrogen and carbon). Clusters with k as large as 20 can be identified in the Ir(#2) spectrum. Note that a 4-keV cluster ion of mass 4000 u has a velocity of only 1.4×10^4 m/s, which is a factor of about four lower than the "threshold" for kinetic electron emission [41,42]. Hence, detection of the large clusters seems to involve some kind of potential emission, presumably associated with the high internal energy carried by cluster ions (see Appendix A). Sub-threshold emission has also been observed with large clusters of pure metal atoms [43]. The spectral features in Fig. 2 suggest that even clusters with $k > 20$ might have been produced but, apart from the limited detection efficiency at masses >4000 u, their identification was hampered by a significant background which appears to be due to fragments produced on-flight along the second half of the tilted drift tube. Furthermore, the width of the cluster peaks increases with increasing k so that separation of the peaks becomes increasingly difficult. Large clusters are also observed in the Ir(#1) spectrum, but for unknown reasons this spectrum exhibits an even higher background than the Ir(#2) spectrum (note the downwards scaling by a factor 10).

Even without a detailed analysis of the measured spectra one can easily tell from the peak positions of the clusters that they must have contained a sizable number of atoms other than iridium. For example, the peak labelled $k = 15$ is centred at m/z 3010. With a mean mass of 192.2 u for Ir, a pure cluster should be centred at m/z 2883. The difference, m/z 127, would correspond to 8 oxygen atoms or about 11 carbon atoms in the $Ir_{15}XY^-$ cluster, i.e., the impurity-to-metal atomic ratio could be between 50% and 70% (even if we disregard the possible presence of hydrogen).

In contrast to the Ir nanoparticle samples, the spectrum recorded for the iridium metal electrode (referred to as IrMet) exhibits clearly detectable clusters only up to $k = 5$, see Fig. 2. In the spectrum of C(Ir) ⟨3 nm⟩ the monomer signal is quite prominent, implying that a significant fraction of the Ir atoms must have been located on rather than in the Ir(C) nanoparticles. The dimer and trimer signals, however, hardly exceed the background level. This is not really surprising. In fact, taking the results for Ir(#1) as a reference, the C(Ir)-to-Ir(#1) yield ratio for Ir_2XY^- is about 0.5%. This is only slightly smaller than the atomic fraction of 0.85% of Ir in C(Ir).

Another important feature of the spectra is that, with the exception of the mass intervals $3 \le m/z \le 11$ and $20 \le m/z \le 23$ (not shown in detail), there is a mass line at every integer mass number. Some important aspects of mass calibration, line shape, background and compositional analysis are discussed in Appendix A.

3.2. Characteristic features of fresh and sputtered samples

A brief look at the spectra in Fig. 2 could impose the impression that the Ir_kXY^- clusters emitted from the different samples are quite similar in terms of the impurity components XY. This is in fact the case for Ir(#1) and Ir(#2), but not for IrMet. For a more detailed discussion, Fig. 3 shows expanded sections of spectra of (a) Ir(#2) and (b) IrMet, for the virgin ("fresh") case (black lines) and after sputtering to the maximum primary ion fluence of about 4×10^{14} (8×10^{14}) ions/cm^2 (grey lines with light-grey filled area). Some of the identified peaks are labelled, indicating the composition of the XY atoms contained in the $IrXY^-$ ions. The spectrum of fresh Ir(#2) is dominated by lines carrying oxygen. In contrast, the oxide lines in the IrMet spectrum are weak, the prominent lines are carbon-rich, of the type $IrC_{p+1}N_q^-$ ($p = 0, 1, 2, \ldots$ and $q = 1, 2$).

The other important difference between the two samples is the response to sputter erosion. The spectral changes observed with IrMet are fairly simple to interpret. As a result of ion bombardment, all secondary ion signals decrease, notably those representing molecules with a large number of XY constituents. The characteristic pattern of the IrMet spectrum, however, did not change markedly in course of sputter erosion. The bombardment induced decrease in secondary ion yield is known to be due to the removal of adsorbates and the (carbon-rich) surface layer [44]. The removal process is commonly referred to as sputter cleaning.

A comparison of the spectra of sputtered Ir(#1) and Ir(#2) for clusters in the range $2 \le k \le 6$ is presented in Fig. 4. The observed

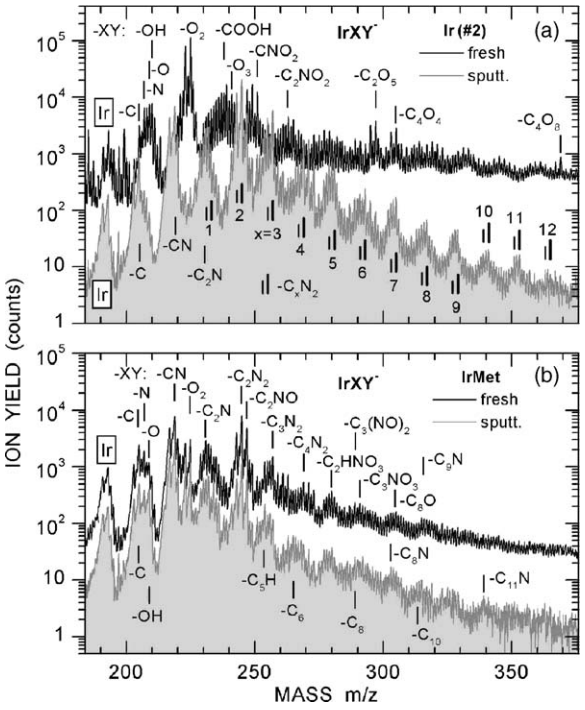

Fig. 3. Comparison of expanded sections of the mass spectra (a) Ir(#2) and (b) a polished iridium reference electrode. The black spectra represent the composition of the fresh samples, the grey spectra were taken after prolonged sputter erosion.

mass lines are mostly due to $Ir_kC_p^-$. For small k, there is also a significant contribution due to $Ir_kC_{p+1}N^-$. Comparatively high signals of this type appear to be largely due to a high ionisation probability brought about by the attachment of CN^- to Ir_kC_p (CN^- is the most prominent line in the spectra, with peak yields up to 1×10^6 counts; not visible in Fig. 2). Note that, similar to the fresh samples, the spectra of the two Ir samples shown in Fig. 4 are largely the same, except for the fact that the ion yields for Ir(#2) are typically a factor three higher that for Ir(#1). This difference is tentatively attributed to the differences in surface coverage indicated by the SEM images in Fig. 1a–d.

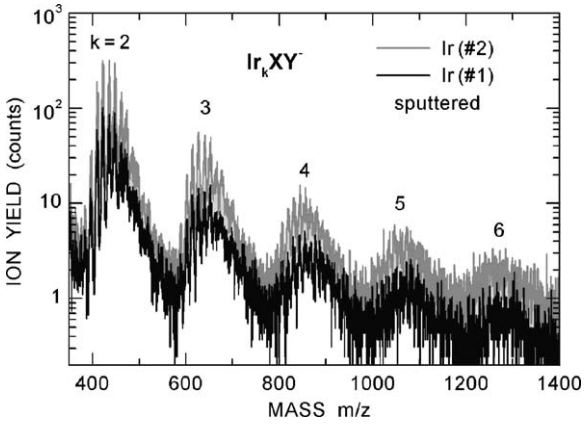

Fig. 4. Comparison of the mass spectra of the two Ir-nanoparticle samples in the intermediate mass range. The spectra depict the sample composition recorded after prolonged sputter erosion.

Returning to Fig. 3a, we note that the spectrum of fresh Ir(#2) features particularly prominent lines due to IrO_2^-. After sputtering these lines have completely disappeared and strong carbon-rich lines dominate the spectrum. Inspection of the spectral features in different mass regions shows that information on sample composition can be derived most directly from large cluster ions. Fig. 5 illustrates this aspect for clusters ions containing four Ir atoms. The spectrum of the fresh Ir(#2) sample exhibits a series of lines which are mostly due to $Ir_4O_n^-$. The observation of a maximum in yield for $n = 5$ appears to suggest that the nanoparticles from which the signals originated were fairly rich in oxygen. This supposition is supported by the fact that pure Ir_4^- cluster ions were not detectable.

Trying to interpret the $Ir_4O_n^-$ spectrum in Fig. 5 in more detail, we make use of experience gained many years ago in studies on molecular ion yields from oxidised metals and semiconductors [45,46]. Data obtained for $k \leq 3$ suggested a "rule" [46] according to which, for an oxide of composition IrO_x, the most prominent cluster ion would be $Ir_kO_{kx+1}^-$. In Fig. 5, the most prominent ion is $Ir_4O_5^-$, i.e., $k = 4$ and $4x + 1 = 5$ so that $x = 1$. Hence, at their surface, the Ir(#2) particles should be composed of IrO. The same information could have been derived from the results for smaller clusters with $k = 1$–3: the maximum yields were found for IrO_2^-, $Ir_2O_3^-$ and $Ir_3O_4^-$, respectively.

Examples of n-distributions of larger cluster ions, with k between 5 and 10, are depicted in Fig. 6a and b. Previous studies on smaller oxide clusters suggested that the yields $Ir_kO_n^-$ may be described, for a fixed k, by Gaussian distributions, with n (or the corresponding mass interval) as a variable [45,46]. The results obtained by fitting to the experimental results on the low-mass side of the peak height distributions are shown in Fig. 6 as dashed lines. The width of the distributions increases with increasing k. An extended set of results is compiled in Fig. 7. One important aspect is that the full width at 10% of the peak height distribution, $\delta M_{0.1}$, exceeds the mean mass of Ir atoms (192 u) for $k \geq 11$. As already mentioned with reference to Fig. 2, the n-distributions start to overlap in this mass range, more so the larger k. Also shown in Fig. 7 is the width $(2\pi)^{1/2}\sigma$ which, after dividing by 16, should equal the mean number, $\langle n \rangle$, of O atoms per Ir atom in the respective cluster (σ^2 is the variance of the

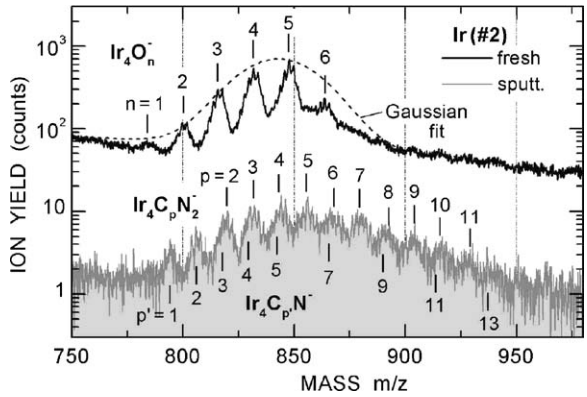

Fig. 5. Expanded section of the mass spectra of fresh and sputtered Ir(#2). The dashed line is a Gaussian fit to the peak-height spectrum of the iridium oxide clusters.

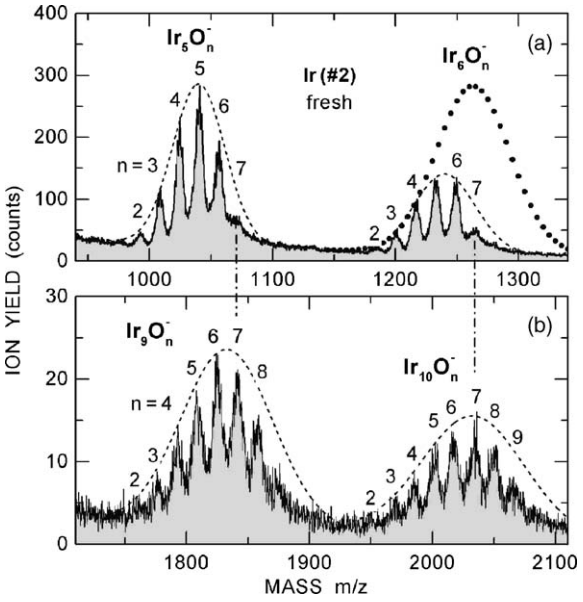

Fig. 6. (a and b) Expanded sections of the mass spectrum of fresh Ir(#2) showing details of the iridium oxide mass lines. The dashed lines are Gaussian fits to the oxide peak heights. The dotted curve in (a) reflects the spectrum that might be observed without preferential loss of oxygen.

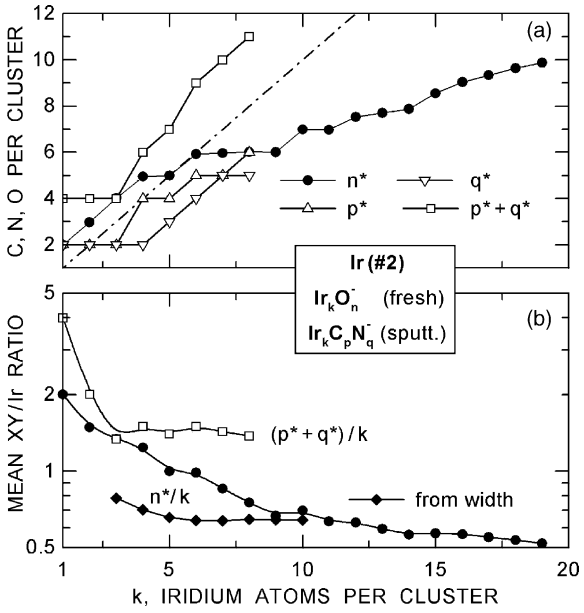

Fig. 8. (a) Number of oxygen, carbon and nitrogen atoms per cluster in the oxide-rich (fresh) and the carbon-rich (sputtered) region of the Ir(#2) sample vs. the number k of iridium atoms in the same cluster. The data relate to the most prominent line in a cluster distribution for a fixed k. (b) The same as (a), but in the form of contaminant-to-iridium ratios.

normal distribution). The linear fit to the data for $k \geq 5$ suggests an apparent (mean) composition IrO_x, with $x = \langle n \rangle / k \cong 0.63$.

As an alternative to the width of the n-distribution we may also use the mass $M_k(n^*)$ of the most prominent peak, relative to the peak position $M_k(n=0)$ of the pure cluster Ir_k^- to determine a "mean" number of oxygen atoms as $n_k{}^* = [M(n^*) - M(n=0)]_k/16$. The data derived from the mass spectrum of fresh Ir(#2) for n^* and n^*/k are depicted in Fig. 8a and b, respectively, as solid circles. For comparison, Fig. 8b also shows the results derived from Fig. 7 (solid diamonds). For $k \geq 9$, the n^*/k ratios derived from the two different approaches agree quite well. For $k \leq 8$, on the other hand, the ratios deviate from each other, more so the smaller the number of Ir atoms per clusters. The difference is tentatively attributed mostly to a cluster-size dependence of the ionisation probability. In the case of a small cluster, the addition of one oxygen atom leads to a large change in composition. Hence, the ionisation potential

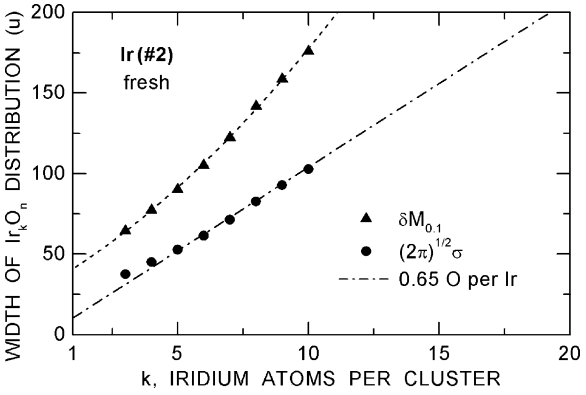

Fig. 7. Width of the peak height distributions of iridium oxide cluster ions vs. the number of iridium atoms per cluster.

(positive ions) or the electron affinity (negative ions) will also change significantly. As a result, one favourable Ir_kO_n configuration will feature a much higher secondary yield than the other ejected configurations with the same k so that, for small k, the n-distribution of ion yields will be comparatively narrow. With large clusters, on the other hand, the addition of one oxygen atom generates only a comparatively small change in the mean composition. Accordingly, one can expect the electron affinity not to change much so that the measured n-distribution will approximately resemble the distribution of all clusters sputtered with the same k. This reasoning also implies that large cluster ions are more representative of the sample composition than small cluster ions.

For large k, the n^*/k ratios in Fig. 8b approach an apparent lower limit of 0.5. Hence, one might be led to the conclusion that the fresh Ir(#2) particles feature a composition of the form IrO_x with $x \cong 0.5$. There are, however, clear indications that this number is smaller than the true value. Inspection of the peak height distributions in Figs. 5 and 6 suggests that, in course of the process of sputtering or soon thereafter, the detected cluster ions suffered from a preferential loss of oxygen. Relevant information on preferential sputtering was previously derived only from changes in the composition of the bombarded surface [47,48]. Here, we are dealing with a different kind of information in that we consider the composition of the sputtered molecules. $Ir_kO_n{}^-$ clusters ejected with a large amount of internal energy may stabilise by rapid release of oxygen atoms. If this takes place within the first few nanoseconds after emission, the oxygen deficient ions will be accelerated to a velocity which, within experimental accuracy, corresponds to the new mass so that the ion will be identified as $Ir_kO_{n-1}{}^-$ or even as $Ir_kO_{n-2}{}^-$ instead of $Ir_kO_n{}^-$. In Figs. 5 and 6, this loss of oxygen appears to be

responsible for the asymmetry of the distributions for different k: the measured peak heights on the high-mass side are distinctly lower than their counterparts on the low-mass side. The actual loss of oxygen might even be larger than suggested by the high-mass difference in yield between the measured and the calculated peak height distributions. A conceivable loss-free distribution is sketched on the right side of Fig. 6a as a dotted curve.

Further evidence for oxygen loss from the ion bombarded nanoparticles may be obtained by inspecting the changes in $Ir_kO_n^-$ ion yield as a function of bombardment fluence, as shown in Fig. 9. All yields decreased with increasing fluence, indicating progressive removal of the material from which the signals originated. However, the initial signal fall-off took place much more rapidly for the yields of the oxygen-rich ions $Ir_4O_5^-$ and $Ir_5O_5^-$ than for the oxygen-poor ions $Ir_4O_3^-$ and $Ir_5O_3^-$. This finding implies that during the initial stage of sample erosion, i.e., up to fluences of about 2×10^{13} ions/cm^2, significantly more O atoms than Ir atoms were sputtered from the nanoparticles. The slopes of the dashed lines representing the roughly exponential initial decay of the oxygen-rich signals is about twice as steep as the decay of the oxygen-poor signals. After the initial period of oxygen depletion, the oxygen-rich signals decay in essentially the same manner as the oxygen-poor signals.

It is worth mentioning that the data presented in Fig. 9 were obtained with an overnight interruption after bombardment to about 1.9×10^{14} ions/cm^2. The spectra recorded the next morning exhibited yields that were only marginally higher than expected on the basis of the trend observed before the interrupt. The small yield enhancement can be attributed to residual gases adsorbed on the sputtered surface during 14-h sample storage in the non-ideal vacuum. The small effect also implies that re-adsorption of released molecules after each step of analysis and sputter erosion can be neglected.

Even though the evidence presented for preferential loss of oxygen is rather convincing, there could be additional reasons for the limited oxygen content of the cluster ions. One possibility is that the Ir nanoparticles featured a metallic core, but were covered with a few monolayers of Ir oxide. Let us assume that the sputtered clusters were compact, i.e., they had roughly the same size in all three directions. Then a cluster containing h atoms will, on the average, contain matter from the top $h^{1/3}$ monolayers of the sample. Under these conditions one would expect the metallic core to give rise to a step in the oxygen-to iridium ratio n^*/k at some critical cluster size k. Such a step is not evident in Fig. 8b, at least not in the size range $k < 20$. Hence, we are led to the conclusion that the analysed Ir nanoparticles were rich in oxygen over a depth exceeding at least three monolayers.

The arguments put forward up to now imply that the cluster ions referred to as $Ir_kO_m^-$ contain only iridium and oxygen. This is not fully true. As discussed in Appendix A, carbon and nitrogen "contamination" of the oxide clusters on the order of 10% can be identified by a detailed peak height analysis.

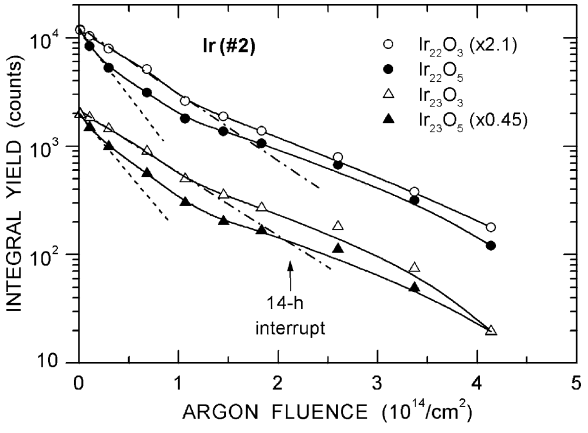

Fig. 9. Fluence dependence of the yield of several iridium oxide cluster ions. The dashed and the dash–dotted lines denote the initial exponential decay of the yields.

3.3. Multi-yield fitting

As shown in Figs. 3, 5 and 8, sputter erosion of the Ir(#2) sample caused a remarkable change of the mass spectra from oxygen-rich to carbon-rich. Clearly, this change in composition calls for a detailed evaluation of the spectral features observed during progressive sample erosion. In order the quantify the contribution of different molecules to the signal at a given mass line it turned out necessary to develop a program that provides simultaneous multi-yield fitting for as many as 40 different XY^- signals associated with atomic or molecular Ir. For simplicity, only the non-protonated secondary ion signals were taken into account. We considered the information contained in the spectrum in the mass range from $M(^{191}Ir_k)$ up to $M(^{191}Ir_k)$ +110 u. To avoid unreasonable scatter in the sometimes low signals observed after significant sputter erosion, the yields are integrated over 10 channels around the peak of each mass line. The number N of input yield data included in the fitting routine depended on the number k of Ir atoms per molecule. For example, for $k = 1$, $N = 48$ and for $k = 3$, $N = 54$. These numbers are determined by the isotopic pattern of Ir_k. To account for sometimes large differences in the yield Y of neighbouring lines, a weight factor $1/Y^2$ was included in the evaluation. The program calculated the optimum integrated yields for the lines due to the two isotopes of Ir or, in the case of Ir_k molecules, to the different combinations of the isotopes.

The procedure becomes transparent by reference to Fig. 10a and b, which show results for fresh and sputtered Ir(#2). The positions of the lines to which the molecule $^{193}IrXY^-$ contributed are marked in panel b. The experimental data are denoted by solid squares. The fit values due to $^{191}IrXY^-$ signals are presented as grey columns, overlaying those due to $^{193}IrXY^-$ (white columns). The sums of the fit values are marked by open triangles. The agreement between the measured and the fitted values is seen to be always quite good, in many cases excellent. In the rare cases in which the sum agrees with (the top of) one of the columns, the measured signal did not suffer from interference (example $^{193}IrO_2^-$ at m/z 225 in Fig. 10a). In most cases, however, interference was quite significant so that the sum was distinctly larger than the major individual contribution.

The mass spectra of molecular ions containing Ir atoms, as in Fig. 10, are not easy to unravel, but they are simple when compared to the spectral regions where the Ir_kXY^- cluster ions

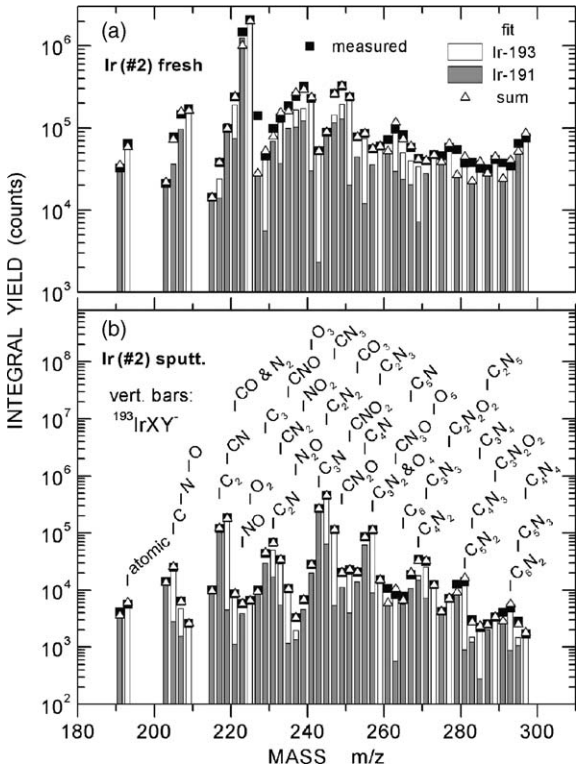

Fig. 10. Multi-yield fitting of the spectral region due to molecular ions containing atomic iridium: (a) fresh and (b) sputtered Ir(#2). In panel (b), the positions of the specified molecules containing Ir-193 are denoted by vertical bars.

were observed. Fig. 11 shows an example for $k = 3$, in which case we had to deal with four combinations of Ir isotopes, denoted in the order of decreasing formation probability as Ir_{12} (a combination of one ^{191}Ir atom and two ^{193}Ir atoms; black column), Ir_{21} (dark grey), Ir_{03} (light grey) and Ir_{30} (white). Most of the mass lines contain contributions from all four permutations, i.e., contributions in white, light grey, dark grey and black.

3.4. Fluence dependence

The information derived from the multi-yield fitting exercise served to identify those mass lines that were best suited for quantifying the removal of oxygen-rich nanoparticle matter

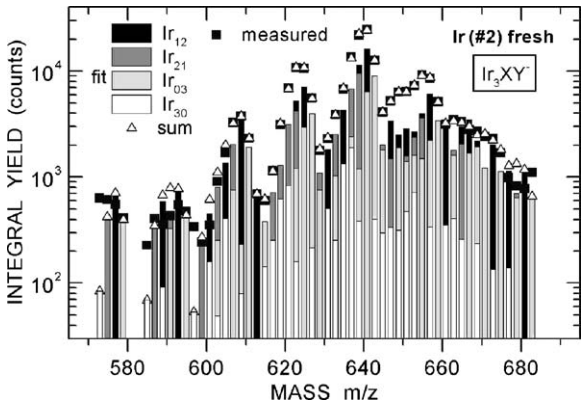

Fig. 11. The same as Fig. 10(a), but for iridium trimers.

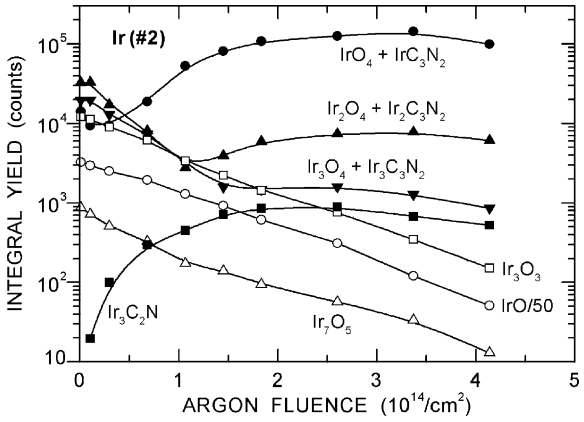

Fig. 12. Fluence dependence of various secondary ions showing examples with and without interference between oxide and carbide lines.

as well as the simultaneous appearance of its carbon-rich counterpart. The argon-fluence dependence of some representative signals observed with Ir(#2) is presented in Fig. 12. In accordance with the results of Fig. 9, those iridium oxide signals, which did not suffer from interference with carbon-rich iridium signals, e.g., $^{193}IrO^-$, $Ir_3O_3^-$ or $Ir_7O_5^-$, exhibited a monotonic decrease by as much as two orders of magnitude. Considering the fact that the data were obtained by eroding a very rough sample of complex morphology, as illustrated in Fig. 1a and b, this comparatively large dynamic range in "depth profiling" is quite surprising. The results suggest that the component of the nanoparticle matter from which the oxide signals originated must have been removed very efficiently by argon bombardment, leaving essentially no residues behind.

As the oxygen-rich signals decrease with increasing primary ion fluence, the "pure" carbon-rich iridium signals, represented by $Ir_3C_2N^-$, increase monotonically, pass through a broad maximum at about 3×10^{14} ions/cm^2 and, at even larger fluence, tend to decrease slightly. If all spectra recorded during sputter erosion are considered, "pure" signals of the type $Ir_kC_pN_q^-$, not suffering from interference with $Ir_kO_n^-$, were rarely found for small k. With few exceptions there was significant interference, i.e., the respective signals reflected both, the initial removal of the oxide and the subsequent appearance of the carbon-rich matter. The resulting complex fluence dependence is exemplified in Fig. 12 by the signals due to $IrO_4 + IrC_3N_2$, $Ir_2O_4 + Ir_2C_3N_2$ and $Ir_3O_4 + Ir_3C_3N_2$. Referring for simplicity to the carbon-rich clusters as "carbides", the carbide-to-oxide yield ratios are seen to decrease with increasing number k of iridium atoms per cluster. This observation could reflect a steady decrease in the ionisation probability of iridium carbide cluster with increasing k. An alternative interpretation might be that with increasing k the sputtered iridium carbide matter is distributed over a larger number p of Ir_kC_p configurations. A positive aspect of these features is that, for large k, the Ir_kO_n signals from Ir(#2) did not suffer from noticeable interference with carbide signals. With Ir(#1), on the other hand, there was a sizable interference ("background") in the upper fluence range.

To illustrate in detail the similarities and differences between the four analysed samples, the integral $IrCN^-$ yields are plotted

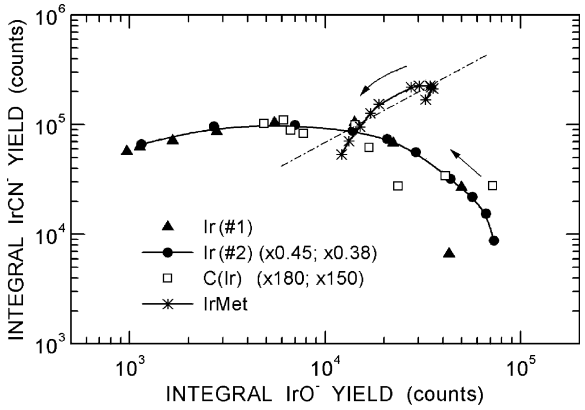

Fig. 13. Correlation between the secondary ion yields of IrCN and IrO. To ease comparison the raw data for Ir(#2) and C(Ir) are multiplied by the scaling factors shown in parentheses. The arrows denote the direction of increasing argon fluence.

in Fig. 13 versus the IrO^- yields. For ease of comparison the yields for Ir(#2) and C(Ir) were multiplied by appropriate factors (first factor applies to IrO^- and second to $IrCN^-$). With very few exceptions, the (scaled) yields for the three nanoparticle samples fall on the same curve. The curve reflects the fact that with increasing primary ion fluence (direction of increasing fluence denoted by arrows) the iridium oxide signals decrease whereas the carbide signals increase up to a maximum and, finally, decrease slowly. These characteristic features are distinctly different from the trend observed with the IrMet reference sample, in which case the oxide and the carbide signals both decrease almost in parallel with increasing fluence (the dash–dotted line represents direct proportionality). Hence, the message is that the nanoparticles have a composition distinctly different from pure metallic iridium covered with surface oxides and carbides.

The scaling factors that had to be applied in order to achieve full compliance for all three sets of nanoparticle data in Fig. 13 were almost the same for IrO^- and $IrCN^-$ (difference only between 20% and 40%). The close similarity of the scaling factors is quite surprising because the two types of secondary ions presumably originated from two different types of nanoparticle matter. At the beginning of ion bombardment, one could have expected significant yield distortions due to the presence of adsorbed hydrocarbons. An effect of this kind appears to be responsible for the deviation of the first (lowest) data point for Ir(#1). Apart from this outlier, the (scaled) yield changes observed with the two Ir samples were identical to within the size of the data points. This agreement leads to the conclusion that the two samples were very similar in composition, but differed in the fractional surface coverage of the filters: taking the mean of the scaling factors, the results suggest that the nanoparticle coverage of Ir(#2) was a factor of $1/0.415 = 2.4$ ($\pm 10\%$) larger than the coverage of Ir(#1). This factor, which reflects the nanoparticle coverage of the filter "seen" by the primary ion beam and the TOF-SIMS instrument, is qualitatively in accordance with the visual impression imposed by the SEM images of Fig. 1. Since the areal mass density of Ir(#1) was even higher than that of Ir(#2), the pronounced differences in fractional filter coverage suggest, as did the SEM images, that local pile-up of nanoparticles was much more pronounced for Ir(#2) than for Ir(#1).

As to the scaling for C(Ir), the applied factor 165 ± 15 is close to the inverse atomic fraction of Ir in the mixed sample, $1/0.0085 = 118$. The agreement of the scaled yields for this sample with the yields for Ir(#1) and Ir(#2) strongly suggests that C(Ir) is composed of a mixture of carbon nanoparticles originating from the carbon electrode and iridium nanoparticles from the Ir electrode. In other words, the particles generated in the spark discharge between the two different electrodes seem to have grown independently. This implies that the original idea of producing carbon nanoparticles containing internally mixed iridium atoms cannot be verified using a spark discharge.

To further substantiate the similarity of the Ir nanoparticles in C(Ir) with those in Ir(#1) and Ir(#2), we take a look at the signals due to hydrocarbon contaminants. As an example, Fig. 14 shows the yields of $COOH(CH_2)_7CO^-$ (m/z 171) versus the IrO^- yields, for three nanoparticle samples and the IrMet reference samples. Rather remarkable is the observation that the initial yields due to hydrocarbon contaminant ions scale almost linearly with the IrO^- yield (the straight dash–dotted line denotes a linear dependence). This finding strongly suggests that the two vastly different secondary ion species originated from the same "source". Apparently, the adsorbed hydrocarbons resided more or less exclusively only on the nanoparticles from which IrO^- ions were emitted. This result is particularly remarkable for C(Ir), in which case almost the whole sample was composed of carbon nanoparticles which would be expected to provide surface sites for adsorption of hydrocarbons in much the same manner as the Ir nanoparticles. The only explanation that might serve to explain the puzzle is that only the Ir oxide and the Ir carbide particles provide sufficient electrical conductivity for undistorted secondary ion emission. Then, of course, all signals should be (roughly) proportional to the fractional coverage of the samples with these particles and, accordingly, the hydrocarbon yield from C(Ir) should be very low, as observed.

To achieve information on the local thickness of the Ir oxide particles, we compare the fluence dependence of oxide and carbide yields in normalised form, i.e., scaled to unity at the

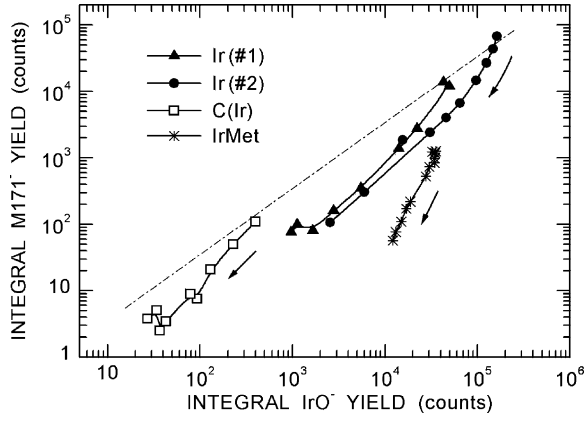

Fig. 14. The same as Fig. 13, but for the hydrocarbon surface contamination at m/z 171 vs. IrO.

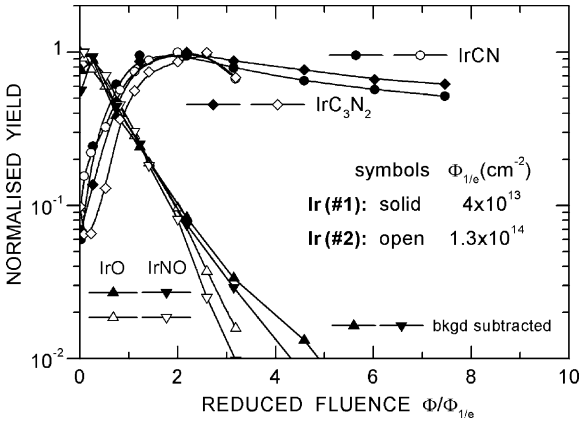

Fig. 15. Normalised yields of iridium oxide and iridium carbide specific secondary ions vs. the reduced argon fluence, for Ir(#1) and Ir(#2).

respective maxima. As one might have expected on the basis of the results in Fig. 13, the results for Ir(#1) and Ir(#2) were found to be quite similar, but on different fluence scales. To account for these differences, the fluence scales were also normalised. The applied scaling factor was the fluence $\Phi_{1/e}$ at which the IrO^- signal had dropped to $1/e$ (=36.8%) of its original value. Fig. 15 illustrates the roughly exponential decrease of oxide signals and the concurrent increase in the carbide signals. In the case of Ir(#1), a background on the order of 1×10^{-2} was subtracted from the as-measured data. This background could be due to either interfering carbide signals (relatively larger than with Ir(#2)) or due to a rather slowly decreasing oxide component. Presented on a reduced fluence scale, the similarities in the sputter removal characteristics of Ir(#1) and Ir(#2) are evident convincingly. This is reasonable results because one would not have expected nanoparticle formation at different spark frequencies to generate material of drastically different composition. However, we are left with two questions that deserve answers: what is the morphology of the presumably two components of the collected nanoparticles that give rise to the "oxide" and the "carbide" signals? Why is the oxide component located on top of the carbide component?

3.5. Assessment of sample structure and morphology

At this point, the only safe statement that can be made concerning the rather mysterious oxide matter is that it is removed by ion bombardment in manner that resembles sputtering of adsorbed monolayers [46,49]. In such a case, the amount of adsorbed material left on the sample as well as the ion yields or measured signals, S, originating from the remaining material usually decrease exponentially with increasing fluence Φ,

$$S(\Phi) = S_0 \exp\left(-\frac{\Phi}{\Phi_{1/e}}\right), \quad (1)$$

where $S_0 = S(\Phi = 0)$. The characteristic fluence $\Phi_{1/e}$ relates to the cross-section σ for monolayer removal [46] as $\Phi_{1/e} = 1/\sigma$ (apparent removal due to bombardment induced damage of the sample is ignored here). The total (integral) yield Σ is simply

$$\Sigma = S_0 \int_0^\infty \exp\left(-\frac{\Phi}{\Phi_{1/e}}\right) = \Phi_{1/e} S_0. \quad (2)$$

The $\Phi_{1/e}$-values were 4×10^{13} and 13×10^{13} ions/cm^2, for Ir(#1) and Ir(#2), respectively. The ratio of the two numbers is 0.31, not much different from the ratio of 0.41 by which the data for the two samples differed in Fig. 13. The close agreement of the two numbers is probably accidental. Instead of being related to the fractional coverage of the filter, as the yields in Fig. 13, $\Phi_{1/e}$ should be closely related to some kind of thickness or size of the sputtered oxide-type nanoparticles. In analogy to Eq. (2), the number N_Σ of atoms removed per unit area by ion bombardment with a sputtering yield Y is [46]

$$N_\Sigma = Y\Phi_{1/e}. \quad (3)$$

For metallic Ir sputtered by 34 keV Ar at 57°, the sputtering yield is estimated from recent studies [50] to be around 10 atoms/ion. Hence, applying Eq. (3) rigorously to the results for oxide removal from Ir(#1), we have $N_\Sigma = 4 \times 10^{14}$ atoms/cm^2. The result would imply that the material from which the Ir oxide signals originated was only about one atomic layer thick, impossibly thin considering the fact that this very material was the source of $Ir_kO_n^-$ cluster ions with k up to 20 (Fig. 2). Even though Eq. (3) relates to monolayer sputtering through the parameter $\Phi_{1/e}$, a relation of the form $N = Y\Phi$ holds quite generally because it is simply the definition of the sputtering yield. Hence, in order to comply with the idea that the oxide layer must feature a reasonable thickness, at least four atomic layers thick, we are led to the conclusion that bombardment induced erosion must have been characterised by an unusually large sputtering yield, on the order of 40 atoms/ion, probably even higher. This enhancement cannot be attributed to the inferred oxidation of iridium because the partial sputtering yield of the metal component in an oxide is generally smaller than the yield of the pure metal [46]. Hence, the high sputtering yield must be related to other properties of the Ir oxide matter that have not been addressed up to now.

The most likely explanation is that we were dealing with very small oxide particles, probably only 1 nm or less in size, i.e., much smaller than the range of the 34 keV Ar^+ ions. Hence, a collision cascade initiated by the primary ion could extend throughout the whole particle so that sputtered atoms could escape in all directions, not just in backward direction as in sputtering of a bulk sample. The scenario has recently been explored by computer simulation, for 100 keV Au incident on a spherical gold nanoparticle with a diameter of 8 nm [51]. In the present context, the most important results were as follows. (i) The mean sputtering yield was 137 atoms/atom, which is larger by a factor of about three than the yield measured for sputtering of bulk metallic gold [52]. (ii) Occasionally, almost complete disintegration of the whole nanoparticle was observed. (iii) During disintegration, a large number of clusters was emitted, with sizes up to 100 atoms. (iv) The low-energy part of the energy distribution of sputtered atoms revealed a thermal contribution of about 18% to the atom emission. (v) The impacts studied revealed

large fluctuations in terms of sputtering yield. The computer simulations may serve to explain three important observations of this study, the high sputtering yield of Ir oxide nanoparticle matter (inferred from the very low characteristic fluence $\Phi_{1/e}$), the emission of large clusters and the apparently high internal energy of the clusters which appeared to have been responsible for preferential loss of oxygen.

Developing the picture of sample composition further, we assume that, in Ir(#1), the Ir oxide was present as one layer of chunks, sheets or flakes on the comparatively large Ir carbide nanoparticles. In such a scenario, the number of atoms in the oxide flakes would be equal to the mean sputtering yield Y. Assuming spherical flakes of diameter D and number density n, the three parameters relate to each other as

$$D = \left(\frac{6Y}{\pi n}\right)^{1/3} \tag{4}$$

Inserting the density of iridium, $n = 71$ atoms/nm^3, we have $D = 0.3Y^{1/3}$ nm, so that, for $Y = 40$, $D = 1.0$ nm. Owing to the power 1/3, reasonable variations of Y (and n) will affect the estimated particle diameter only little. Chunks, flakes or sheets with a size of 1 nm or less could not be detected by the electrical mobility analyser employed to measure particle size distributions during sample preparation. The analyser featured a lower limit of detection of 10 nm [33]. Even with the best currently available mobility analysers, 1-nm objects will be hard to measure in a quantitative manner. Such objects are also well below the lateral resolution of the employed scanning electron microscope and may be identifiable with the best SEM only under ideal conditions [53] (Fig. 16).

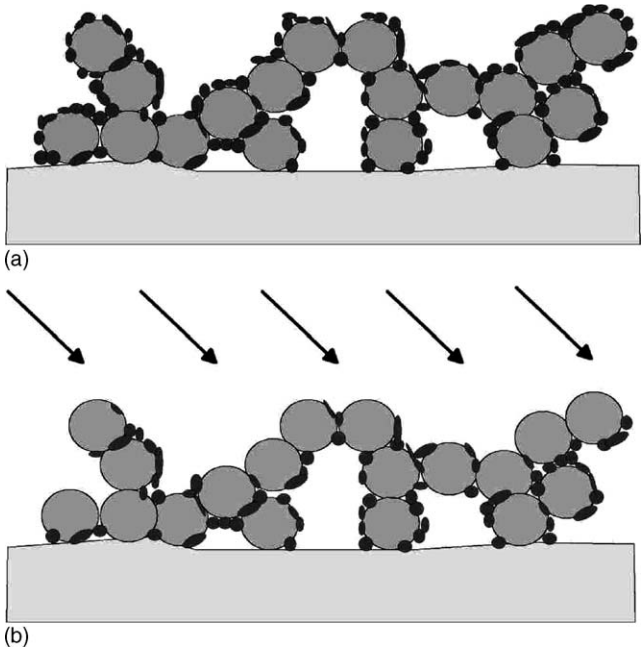

Fig. 16. Schematic illustration of the composition and morphology of Ir(#1), as suggested by the results of this study. The small, dark-grey objects denote the iridium oxide particles, presumably chunks and flakes, the iridium carbide particles are represented by the medium-grey circles. (a) Fresh sample and (b) after exposure to about three times the characteristic fluence.

Based on these results, the composition and morphology of the Ir(#1) sample may have come close to the structure sketched in Fig. 16a. The Ir oxide matter is represented by small, dark-grey objects of somewhat irregular shape, condensed on much larger Ir carbide nanoparticles (light-grey), which are assumed to have had an almost spherical form. After bombardment to a fluence of $3\Phi_{1/e}$, almost all of the oxide matter seen by the primary beam had been removed according to Fig. 15. This status of the sample is illustrated in Fig. 16b (for simplicity we have assumed negligible erosion of the carbide particles). In this kind of picture of sample morphology, the main difference in sample Ir(#2) would be a larger pile-up or a larger size of the oxide particles, so as to give rise to a 3.3-fold (=13/4) rise in the characteristic fluence $\Phi_{1/e}$. Recalling the differences in contrast in the SEM images of Fig. 1, the bombardment induced removal of the "haze" in the images of fresh Ir nanoparticles might well reflect sputter erosion of the oxide flakes.

3.6. Some aspects of spark-discharge nanoparticle generation

Given the fact that the basic processes contributing to particle formation in a spark discharge are not known in any detail presently, we like to outline some ideas as to the origin of the two types of particles inferred from this study. Presumably, the differences are due to the action of two processes of sample removal, i.e., sublimation and sputtering. After ignition of a spark, the gas in the volume between the electrodes will be ionised. Depending on their charge state and the magnitude of the electric field, the ions will be accelerated to the electrode of opposite charge, causing sputter erosion of that electrode. One would expect sputtering to be mostly due to ions (Ar^+) of the gas in which the electrodes are immersed, but both positive and negative ions can also be produced from C and Ir atoms released by sublimation. Even though spark discharge particle production was carried out in a flow of high-purity argon, this approach does not prevent the availability of sufficiently high concentrations of oxygen and carbon for reactions with emitted iridium atoms and molecules. SIMS studies have shown that even in an ultra-high vacuum environment ($\sim 1 \times 10^{-10}$ mbar), condensation of molecules containing hydrogen, carbon, nitrogen and oxygen is readily observable [54].

Inspection of the electrodes after prolonged operation suggests that both of them are eroded, though with different efficiency. The supposition is that the pathways of condensation and agglomeration are different for the matter released from the electrodes of different polarity. The local temperature during emission can be expected to be an important parameter and the temperatures are probably distinctly different at the "sublimation" and the "sputtering" electrode. Hence, it would not be surprising if one side were to favour reaction with oxygen, the other with carbon. The resulting molecules and atoms are likely to agglomerate rapidly before they are carried away in the flow of argon. The agglomeration processes taking place further downstream may favour reactions between chemically similar clusters, to the end that flakes and nanoparticles are formed, which contain mostly oxides or carbides. Only by the time that

most of the smaller cluster-type units have reacted, oxide flakes will start to condense on carbide nanoparticles. However, it cannot be excluded that a significant fraction of the oxide flakes will come to rest on the carbide nanoparticles only during collection on the filter.

4. Conclusions

As one could have expected from the SEM images of the collected spark-generated nanoparticle matter, TOF-SIMS analysis generated very complex mass spectrometric information. Data analysis turned out to be particularly difficult because the spectra changed rather strongly in course of sample erosion by ion bombardment. Two major components were identified in the Ir containing matter, one rich in oxygen with minor contributions due to carbon and nitrogen, the other rich in carbon, with significant contributions due to nitrogen. Compositional analysis was facilitated by the observation of unusually large Ir_kXY^- cluster ion yields, notably for the oxygen-rich component, with k up to 20. The other important result was that the oxide cluster ions disappeared very rapidly as a result of ion bombardment. Taken together the two types of information suggested that the Ir oxide matter must have been contained in objects with a size of 1 nm or less, much smaller than the Ir carbide nanoparticles.

The results may be of considerable significance for animal studies on health effects due to inhaled nanoparticles. The inferred very high sputtering yields of the oxide flakes imply that, on target, they were loosely bound to the carbide nanoparticles. Once inhaled, they may be able to stray around in the lung in a manner that may differ distinctly from what is accessible to the carbide nanoparticles. Considering the fact that the mass contained in the Ir oxides is probably small compared to the Ir carbides, the observed relocation of Ir matter into the blood and body organs [29,30] may be largely be due to the oxide flakes rather than the "real" carbide nanoparticle. This could lead to a pronounced overestimate of the efficiency of nanoparticle translocation. The results presented here and elsewhere [33] strongly suggest that the mere characterisation of laboratory generated nanoparticles by their electrical mobility diameter can be strongly misleading if one aims at determining the size dependence of particle translocation.

In the future, much work will be required to really understand the processes governing nanoparticle generation in a spark discharge. The previous approach to characterise only the apparent end-product of this process (e.g., by TEM) needs to be extended considerably. Advanced characterisation may also pave the way towards refinements of the spark-discharge particle-production process. Desirable modifications of particle composition and shape may be possible by the controlled addition of "reactive" gases like oxygen, carbon dioxide or the like to argon or nitrogen. This study has shown that particle analysis by an advanced surface analytical technique like TOF-SIMS is needed if one wants to characterise the products of spark-discharge particle formation as completely as possible. Controlled sputter erosion turned out to be an indispensable part of the analysis. Considering the very special phenomena described here, i.e., the strongly enhanced sputtering yields of Ir oxide flakes, future studies should be particularly valuable if ion beams of comparatively high energy are being used.

Appendix A

In order to identify large cluster ions as accurately as possible, particular attention had to be devoted to mass calibration. Considering the fact that the employed TOF system did not include means for energy focussing, only ions with a low energy of ejection were suited for mass calibration. Complex molecular ions originating from adsorbed organic contaminants, like $COOH(CH2)_u$, $COOH(CH2)_uCO^-$ or $COOH(CH2)_uCNO^-$, with $u = 0, 1, 2, \ldots$, turned out to be particularly useful. Mass calibration was based on the idea of assigning a negligible mean kinetic energy E to these large molecular ions, i.e., we set $E = 0$. The approach appears to be justified because the most probable energy of very similar ions sputtered from thin films of polyethylene terephthalate (PET) was found to be about 2 eV [55]. For less strongly bound adsorbed molecules, one can expect an even lower ejection energy. The calibration exercise showed that, at m/z below about 350, mass peaks featuring mass differences by 0.01 u can be distinguished rather safely (corresponding to a spacing by half a channel in the TOF spectrum).

Aspects of line width and line shape may be discussed with reference to Fig. 17. The half width, $\delta M_{0.5}$, of the lines is 0.40 u, see background corrected lines centred at m/z 304.94. The contribution, δM_t, to the mass resolution, set by the time resolution δt (pulse width 3 ns), the effective drift length of the TOF system (68 cm) and the energy E in the drift tube (4 keV) is $\delta M_t = 2(\delta t/t)M = 9 \times 10^{-3} M^{1/2}$, so that, for $M = 305$ u, $\delta M_t = 0.16$ u. The broadening δM_E due to the intrinsic width, δE, of the energy distribution of the sputtered atoms or molecules is, for $\delta E = 3$ eV [55], $\delta M_E = -(E/E)M = 0.75 \times 10^{-3} M$ or $\delta M_E(M = 305) = 0.23$ u. Summing up the two contributions in quadrature, the calculated total mass resolution is $\delta M_{t,E} = 0.28$ u, distinctly smaller than the measured half width. The difference suggests that a third contribution to the line width needs to be included, the kinetic energy release, δE_f, in unimolecular fragmentation [56],

$$\delta E_f = \left(\frac{4M'M''\varepsilon E}{M^2} \right)^{1/2}, \tag{A.1}$$

where ε is the kinetic energy release, M the mass of the parent ion, and M' and M'' are the masses of the ion and the neutral fragment. Let us assume that the mass of one fragment is very small compared to the other, say $M'' \ll M'$, so that $M' \approx M$. Then, with $E = 4$ keV, $\delta E_f \approx 126(\varepsilon M''/M)^{1/2}$ and, with $M = 305$ u, $\delta E_f \approx 7.2(\varepsilon M'')^{1/2}$. To produce $\delta E_f = \delta E = 3$ eV, we must have $\varepsilon = 0.16/M''$, i.e., $\varepsilon = 0.16$ and 0.01 eV for $M'' = 1$ and 16 u, respectively. The calculated released energies are well within the range of typical values (0.002–2 eV [56]).

A significant contribution of the kinetic energy release to the total line width implies that the respective lines are broadened symmetrically. This notion is substantiated by a detailed analysis of the narrow spectrum in Fig. 17. The mass lines can be described by normal (Gaussian) distributions, as shown by the

dotted curve centred at *m*/*z* 304.94. To achieve a perfect fit (solid line) to the measured spectrum (solid circles), one has to assume a non-constant background with a height defined by the minima between the measured peaks (bkgd A, dashed line). It is much more likely, however, that within the narrow mass range covered by Fig. 17, the background was approximately constant, as indicated by the dash–dotted line (bkgd B, dash–dotted line). Then a fit of the same quality as above (agreement within the thickness of the solid lines) requires that all mass lines feature a significant symmetrical broadening in the tails (dash–dotted curve centred at *m*/*z* 304.94). This finding supports the idea that kinetic energy release constitutes a significant contribution to the line width. The observation that the effect is predominantly showing up in the tails of the mass line leads to the reasonable conclusion that only about 20–30% of the signal observed at a certain mass line was due to decomposed fragments. The remainder of the parent ions must have survived fragmentation by the time-of-arrival at the detector.

The data in Fig. 17 may also serve to illustrate the procedure that may be used for peak identification. First we recall that iridium features two isotopes, ^{191}Ir and ^{193}Ir, with, respectively, masses of 190.961 and 192.963 u and isotopic abundances of 37.30% and 62.70%. The two pairs of lines at about *m*/*z* 302 and 304 and 303 and 305 suggest that they are mostly due to molecules containing Ir atoms and a combination of H, C, N and O. Subtracting the isotopic masses from the fitted (three-decimal) peak positions of the two pairs of mass lines, the differences turn out to be 110.996 and 111.980 u (±0.003 u). These numbers agree within the third decimal with the masses of C_4NO_3H and C_4O_4, respectively. The conclusion is that, in spite of the limited mass resolution, accurate mass calibration in combination with peak fitting provides means for a rather save assignment of the major contribution to the measured mass lines.

Making use of the isotopic pattern of Ir in larger clusters one can derive detailed information on cluster composition. An example is presented in Fig. 18, which shows a section of the

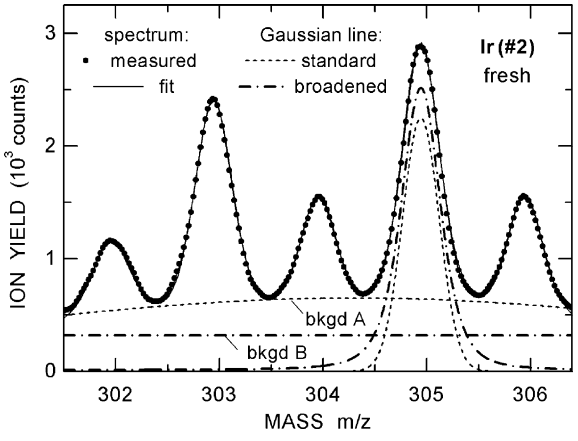

Fig. 17. Expanded section of the TOF mass spectrum of fresh Ir(#2) (solid circles). The two (indistinguishable) solid lines through the experimental data are fit functions derived under the assumption that the spectrum is composed of symmetrical lines and a background. The dashed and the dash–dotted lines illustrate two alternative approaches.

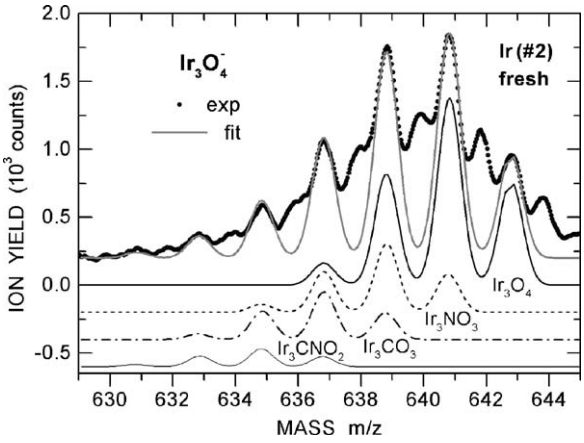

Fig. 18. Decomposition of the mass spectrum of a contaminated iridium oxide cluster ion into the pure oxide spectrum and the nitrogen and carbon containing contributions.

spectrum of fresh Ir(#2), which is grossly described as representing an Ir_3O_4 cluster. If this were true, the statistics of Ir_3 formation from ^{191}Ir and ^{193}Ir would result in the calculated spectrum labelled Ir_3O_4 (solid black curve). The two peaks at *m*/*z* 638.86, due to Ir_{21} (i.e., two isotopes of ^{191}Ir and one of ^{193}Ir) and at *m*/*z* 642.87, due to Ir_{03} (three isotopes of ^{193}Ir), should have almost the same height. In the measured spectrum, however, the first of the two peaks is almost a factor of two higher than the second (measured with respect to an assumed constant background level of 240 counts). This difference implies that the measured spectrum also contains a sizable contribution due to Ir_3NO_3 (short-dashed line). The procedure needs to be extended to include at least a third contribution due to Ir_3CO_3 (or $Ir_3N_2O_2$), dash–dotted line. The two added contributions exhibit the same pattern of peak heights as Ir_3O_4, but are shifted to lower masses by $\Delta M = 1.99$ and 3.99 u, respectively. To get good agreement at *m*/*z* 632.86 and 634.82 one would have to include Ir_3CNO_2 (not shown). Accounting for the different contributions to the total signal, the atomic fraction of C + N in the sum C + N + O turned out to be about 12%. Performing the same kind of analysis with the clusters referred to as Ir_4O_5 and Ir_5O_5, the C + N fractions were found to be 8% and 6%, respectively, i.e., the C + N fraction decreased with increasing cluster size. The decrease suggests that the two species were not present in the bulk of the nanoparticles but originated from organic contaminants adsorbed at the surface. This interpretation is supported by the trend observed with ion signals that have not been discussed up to now, the protonated species which give rise to the peaks at masses $M + 1$. In Ir_3O_4, the height of these peaks, which were not included in the peak fitting procedure of Fig. 18, amounts to about 60% of the lines at M. In Ir_4O_5, the protonated peaks amount to only about 20% of the non-protonated peaks and in Ir_5O_5 they were difficult to identify. The observed size dependence of the apparent contamination of molecular secondary ion signals supports the notion that information on the chemical composition of a sample may best be derived from large clusters.

References

[1] M.O. Andreae, C.D. Jones, P.M. Cox, Nature 435 (2005) 1187.
[2] D.W. Dockery, C.A. Pope III, X. Xu, J.D. Spengler, J.H. Ware, M.E. Fay, B.G. Ferriss, F.E. Speizer, N. Engl. J. Med. 329 (1993) 1753.
[3] R.M. Harrison, R.E. van Grieken (Eds.), Atmospheric Particles, John Wiley & Sons, Chichester, 1998.
[4] L.M. Brown, N. Collings, R.M. Harrison, A.D. Maynard, R.L. Maynard (Eds.), Philos. Trans. R. Soc. Lond. A358 (2000) 2563.
[5] H. Burtscher, S. Künzel, C. Hüglin, J. Aerosol Sci. 29 (1998) 389.
[6] D.B. Kittelson, J. Aerosol Sci. 29 (1998) 575.
[7] M. Kalberer, D. Paulsen, M. Sax, M. Steinbacher, J. Dommen, A.S.H. Prevot, R. Fisseha, E. Weingartner, V. Frankevich, R. Zenobi, U. Baltensperger, Science 303 (2004) 1659.
[8] G. Oberdörster, E. Oberdörster, J. Oberdörster, Environ. Health Perspect. 113 (2005) 823.
[9] S. Schwyn, E. Garwin, A. Schmitt-Ott, J. Aerosol Sci. 19 (1988) 639.
[10] C. Helsper, W. Mölter, F. Löffler, C. Wadenpohl, S. Kaufmann, G. Wenninger, Atmos. Environ. 27A (1993) 1271.
[11] C. Roth, G.A. Ferron, E. Karg, B. Lentner, G. Schumann, S. Takenaka, J. Heyder, Aerosol Sci. Technol. 38 (2004) 228.
[12] D. Mark, in ref. [3], Chap.
[13] M. Wentzel, H. Gorzawski, K.-H. Naumann, H. Saathoff, S. Weinbruch, J. Aerosol Sci. 34 (2003) 1347.
[14] A. Laskin, J.P. Cowin, Anal. Chem. 73 (2001) 1023.
[15] T. Junno, S. Anand, K. Deppert, L. Montelius, L. Samuelson, J. Aerosol Sci. 27 (1996) S173.
[16] H. Sato, T. Ohtsu, I. Komasawa, J. Colloid Interface Sci. 230 (2000) 200.
[17] L.A. Sgro, G. Basile, A.C. Barone, A. D'Anna, P. Minutolo, A. Borghese, A. D'Alessio, Chemosphere 51 (2003) 1079.
[18] G. Köllensperger, G. Friedbacher, R. Kotzick, R. Niessner, M. Grasserbauer, Fresenius J. Anal. Chem. 364 (1999) 296.
[19] U. Kirchner, R. Vogt, C. Natzeck, J. Goschnick, J. Aerosol Sci. 34 (2003) 1323.
[20] N. Klaus, Sci. Total Environ. 31 (1983) 263.
[21] J. Goschnick, J. Schuricht, H.J. Ache, Fresenius J. Anal. Chem. 350 (1994) 426.
[22] J. Goschnick, C. Natzeck, M. Sommer, Appl. Surf. Sci. 144–145 (1999) 201.
[23] P. Konarski, I. Iwanejko, A. Mierzejewska, A. Wymysłowski, Vacuum 63 (2001) 685.
[24] J. Zehnpfennig, H.G. Cramer, T. Heller, E. Niehuis, H. Rulle, T. Stephan, A. Benninghoven, in: A. Benninghoven, Y. Nihei, R. Simizu, H.W. Werner (Eds.), Secondary Ion Mass Spectrometry SIMS IX, John Wiley & Sons, Chichester, 1994, p. 453.
[25] P.K. Chu, R.W. Odom, D.F. Reich, Mater. Chem. Phys. 43 (1996) 87.
[26] R.E. Peterson, B.J. Taylor, Atmos. Environ. 36 (2002) 6041.
[27] P. Lazzeri, G. Clauser, E. Iacob, A. Lui, G. Tonidandel, M. Anderle, Appl. Surf. Sci. 203–204 (2003) 767.
[28] A. Laskin, D.J. Gaspar, W. Wong, S.W. Hunt, J.P. Cowin, S.D. Colson, B.J. Finlayson-Pitts, Science 301 (2003) 340.
[29] W.G. Kreyling, M. Semmler, F. Erbe, P. Mayer, S. Takenaka, H. Schulz, G. Oberdörster, A. Ziesenis, J. Toxicol. Environ. Health A65 (2002) 1513.
[30] M. Semmler, J. Seitz, F. Erbe, P. Mayer, J. Heyder, G. Oberdörster, W.G. Kreyling, Inhal. Toxicol. 16 (2004) 453.
[31] W.P. Krekelberg, J. Greely, M. Mavrikakis, J. Chem. Phys. B108 (2004) 987.
[32] S. Musić, S. Popović, M. Maljković, Ž Skoko., K. Furić, A. Gajović, Mater. Lett. 57 (2003) 4509.
[33] K. Wittmaack, J. Nanoparticle Res., doi:10.1007/s11051-006-9127-0.
[34] N. Menzel, P. Schramel, K. Wittmaack, Nucl. Instrum. Methods Phys. Res. B 189 (2002) 94.
[35] T. You, O. Niwa, R. Kurita, Y. Iwasaki, K. Hayashi, K. Suzuki, S. Hirono, Electroanalysis 16 (2004) 54.
[36] W. Szymczak, K. Wittmaack, Nucl. Instrum. Methods Phys. Res. B88 (1994) 140.
[37] K. Wittmaack, W. Szymczak, G. Hoheisel, W. Tuszynski, J. Am. Soc. Mass Spectrom. 11 (2000) 553.
[38] W. Szymczak, K. Wittmaack, Rapid Commun. Mass Spectrom. 16 (2002) 2025.
[39] W. Szymczak, K. Wittmaack, Appl. Surf. Sci. 203–204 (2003) 170.
[40] K. Wittmaack, Atmos. Environ. 39 (2005) 1173.
[41] L.A. Dietz, J.C. Sheffield, J. Appl. Phys. 46 (1975) 4361.
[42] E.V. Alonso, R.A. Baragiola, J. Ferrón, M.M. Jakas, A. Oliva-Florio, Phys. Rev. B22 (1980) 80.
[43] A. Wucher, personal communication, 2006.
[44] K. Wittmaack, Int. J. Mass Spectrom. Ion Phys. 17 (1975) 39.
[45] C. Plog, L. Wiedmann, A. Benninghoven, Surf. Sci. 67 (1977) 565.
[46] K. Wittmaack, Surf. Sci. 89 (1979) 668.
[47] I. Betóti, R. Kelly, M. Mohai, A. Tóth, Nucl. Instrum. Methods Phys. Res. B 80–81 (1993) 1219.
[48] H. De Witte, T. Conrad, W. Vandervorst, R. Gijbels, Appl. Surf. Sci. 203–204 (2003) 523.
[49] A. Benninghoven, Surf. Sci. 35 (1973) 427.
[50] M.P. Seah, C.A. Clifford, F.M. Greeen, I.S. Gilmore, Surf. Interface Anal. 37 (2005) 444.
[51] R. Kissel, H.M. Urbassek, Nucl. Instrum. Methods Phys. Res. B 180 (2001) 293.
[52] S. Bouneau, A. Brunelle, S. Della-Negra, D. Jacquet, Y. Le Beyec, M. Pautrat, H.H. Andersen, Phys. Rev. B 65 (2002) 144106.
[53] J. Cazaux, J. Microsc. 217 (2005) 16.
[54] K. Wittmaack, Nucl. Instrum. Methods 218 (1983) 327.
[55] A. Delcorte, X. Vanden Eynde, P. Bertrand, D.F. Reich, Int. J. Mass Spectrom. 189 (1999) 133.
[56] J. Laskin, C. Lifshitz, J. Mass Spectrom. 36 (2001) 459.